


Impacts of pre-initial conditions on anisotropic separate universe simulations: a boosted tidal response in the epoch of reionization

Shogo Masaki^{1,2} , Takahiro Nishimichi^{3,4} and Masahiro Takada⁴

¹*Department of Mechanical Engineering, National Institute of Technology, Suzuka College, Suzuka, Mie 510-0294, Japan*

²*Department of Physics, Nagoya University, Nagoya, Aichi 464-8601, Japan*

³*Center for Gravitational Physics, Yukawa Institute for Theoretical Physics, Kyoto University, Kyoto 606-8502, Japan*

⁴*Kavli Institute for the Physics and Mathematics of the Universe (WPI), The University of Tokyo Institutes for Advanced Study (UTIAS), The University of Tokyo, Kashiwa, Chiba 277-8583, Japan*

13 June 2022

ABSTRACT

To generate initial conditions for cosmological N -body simulations, one needs to prepare a uniform distribution of simulation particles, so-called the pre-initial condition (pre-IC). The standard method to construct the pre-IC is to place the particles on the lattice grids evenly spaced in the three-dimensional spatial coordinates. However, even after the initial displacement of each particle according to cosmological perturbations, the particle distribution remains to display an artificial anisotropy. Such an artifact causes systematic effects in simulations at later time until the evolved particle distribution sufficiently erases the anisotropy. In this paper, we study the impacts of the pre-IC on the anisotropic separate universe simulation, where the effect of large-scale tidal field on structure formation is taken into account using the anisotropic expansion in a local background (simulation volume). To quantify the impacts, we compare the simulations employing the standard grid pre-IC and the glass one, where the latter is supposed to suppress the initial anisotropy. We show that the artificial features in the grid pre-IC simulations are seen until $z \sim 9$, while the glass pre-IC simulations appear to be stable and accurate over the range of scales we study. From these results we find that a coupling of the large-scale tidal field with matter clustering is enhanced compared to the leading-order prediction of perturbation theory in the quasi non-linear regime in the redshift range $5 \lesssim z \lesssim 15$, indicating the importance of tidal field on structure formation at such high redshifts, e.g. during the epoch of reionization.

Key words: large-scale structure of Universe – cosmology: theory

1 INTRODUCTION

Ongoing and future galaxy surveys such as the Subaru Hyper Prime-Cam survey (Aihara et al. 2018), the Subaru Prime Focus Spectrograph survey (Takada et al. 2014), the ESA Euclid mission (Laureijs et al. 2011), the Rubin Observatory Legacy Survey of Space and Time¹, and the NASA Nancy Grace Roman Space Telescope mission (Spergel et al. 2015), would map galaxies in the Universe with an unprecedented statistical precision in a larger volume than ever. The underlying matter distribution, inferred from the observed distribution of galaxies, contains key information about fundamental problems in cosmology such as the nature of dark matter and dark energy. To extract such information from

the observed galaxy distribution in an unbiased way, we need to accurately model the evolution of matter clustering in the linear and non-linear regimes as well as dark matter halo-galaxy connections provided a background cosmological model and the initial conditions of primordial perturbations.

Several works have shown that the long-wavelength gravitational potential fields with wavelengths comparable with or greater than the size of a survey volume, so-called supersurvey modes, cause non-trivial effects in large-scale structure; they affect the growth of structures in the finite-volume survey region, and cause statistical scatters to clustering observables measured from the survey region (Hamilton et al. 2006; Sato et al. 2009; Takada & Hu 2013). To study the effects of supersurvey modes, a useful simulation based method, called “separate universe (SU) simulation technique”, has been developed (Sirko 2005; Li et al.

* shogo.masaki@gmail.com

¹ <https://www.lsst.org>

2014; Wagner et al. 2015; Baldauf et al. 2016; Takahashi et al. 2019; Barreira et al. 2019; Chan et al. 2020; Barreira et al. 2020). There are two effects of the supersurvey modes reflecting the fact that the effects are characterized by the Hessian matrix of the long-wavelength gravitational potential field. The first effect is from the averaged over- or under-density contrast in the finite-volume region, which is defined by the trace part of the Hessian matrix or the Laplacian of the long-wavelength gravitational potential field. In the separate simulation technique, the effect of supersurvey density contrast can be absorbed into the change of the background Friedman-Robertson-Walker (FRW) expansion; e.g., if a given survey region is embedded into a slightly over-density region, the effect on the structure formation can be described by using the local FRW background with the slightly positive curvature. This SU simulation can fully take into account the mode-coupling of the supersurvey mode with subsurvey (or subbox) modes, including the non-perturbative effects such as formation of halos.

The second supersurvey effect arises from the large-scale tidal field that is the trace-less part of the Hessian matrix (Ip & Schmidt 2017; Akitsu et al. 2017; Barreira & Schmidt 2017; Akitsu & Takada 2018; Li et al. 2018). In the SU simulation technique, this effect can be included by introducing a local background with *anisotropic* expansion (hereafter simply ASU simulation to refer the anisotropic SU simulation), because the isotropic FRW background does not contain such a degree-of-freedom of the anisotropic expansion. This ASU simulation technique was only recently developed by a few groups, initially by Schmidt et al. (2018) based on a particle-mesh method and recently by Stücker et al. (2020) and Masaki et al. (2020) based on the Tree-Particle-Mesh (TREEPM) code. These SU simulations are very useful, because they allow one to keep a high numerical resolution in a small box to simulate non-linear structure formation by running sets of simulations with the same initial seeds, but with different supersurvey modes (e.g. see D’Aloisio et al. 2020, for such a study). Such SU simulations are equivalent to running the simulations in a much larger volume with the same numerical resolution and extracting a small region comparable to the target observed volume, which might be infeasible due to the numerical expensiveness.

In this paper, we study how inaccuracies in the initial conditions of ASU simulations cause possible artificial effects in the simulated structure formation. In order to generate the initial conditions for cosmological simulations, we need pre-initial conditions (pre-ICs), which refer to “homogeneous and isotropic” distributions of simulation particles, on top of which a small displacement is given to each particle according to the cosmological model of interest. However, achieving a high degree of homogeneity as well as isotropy in a pre-IC with a finite number of particles is not obvious. A commonly-used method is the grid-based pre-IC (e.g., Efstathiou et al. 1985), where particles are placed on the lattice grids evenly spaced in the three-dimensional coordinates. In this case, however, the particle distributions are anisotropic, making the three Cartesian axes special directions. Since we are interested in the effect of large-scale tidal field on structure formation, which is anisotropic by nature, the anisotropy of grid-based pre-IC might cause artificial, systematic errors in the ASU simulation results at later time, as discussed in Stücker et al. (2020).

To study the impact of pre-IC on ASU simulation, we employ the glass-based pre-IC (White 1993; Baugh et al. 1995; White 1996), where pre-IC anisotropies of particle distribution are expected to be suppressed. There are several attempts to investigate possible advantages of glass pre-ICs over grid (e.g., Baugh et al. 1995; Crocce et al. 2006; L’Huillier et al. 2014). In most of the works, the interest is in the evolution of isotropic statistical quantities such as the standard non-linear matter power spectrum. Furthermore, some authors have proposed alternative approaches such as a quaquaversal tiling (Hansen et al. 2007) or the capacity constrained Voronoi tessellation (CCVT) (Liao 2018) to overcome the shortcomings of grid or glass pre-ICs. While the conclusions of these earlier investigations depend on the precise setting of the experiment or the target quantities, in general, a clear and significant disadvantage of grid pre-ICs in practical applications over alternative methods has not been reported for cold dark matter cosmologies (also see Wang & White 2007, for hot/warm dark matter cosmologies). Nevertheless, the artificial pattern of grid pre-ICs is known to source a spurious anisotropic force field, which can be evaluated analytically by treating the displacements from a pre-IC as small variables, known as *particle linear theory* (PLT; Marcos et al. 2006). The consequences of grid pre-ICs on the growth of structures in the linear and quasi non-linear regimes were also quantified within the PLT framework (Joyce & Marcos 2007; Joyce et al. 2009). Such artificial anisotropies inherent in grid pre-ICs could be more problematic if one’s interest lies in the evolution of anisotropic statistical quantities.

In this paper, we study the benefit of glass-based ICs for ASU simulations, comparing with the results from grid-based ICs. To evaluate the performance of glass-based ICs, we study the *tidal response* function of the matter power spectrum (Schmidt et al. 2018), which describes the anisotropic growth of structures under the influence of a large scale tidal field, as a function of wave vector. Since there is the leading-order prediction of perturbation theory (PT) (hereafter simply the PT prediction) for the tidal response (Akitsu et al. 2017; Barreira & Schmidt 2017; Akitsu & Takada 2018), we first check the performance of simulation results against this PT prediction in small k bins or at higher redshifts. Then we carefully study the tidal response function over an intermediate range of scales in the quasi non-linear regime, lying between the linear and highly non-linear regimes. We show that the tidal response has a boosted amplitude, compared to the PT prediction, at such intermediate scales in the high redshift range of $5 \lesssim z \lesssim 15$, indicating the importance of large-scale tidal field on the early phase of structure formation, e.g. during the epoch of cosmic reionization. We also show that the anisotropy of grid pre-ICs indeed causes an artificial error in the tidal response at $z \gtrsim 9$, where the initial conditions still have a relatively large impact on the simulated structures.

The rest of this paper is organised as follows. In Sec. 2, we briefly review the effects of the tidal field due to the supersurvey modes and ASUs. In Sec. 3, we discuss the pre-ICs used in this work and explain the details of our simulations. The results are presented in Sec. 4. We study the tidal response measured from simulations with the grid- and the glass-based pre-ICs at both high- z and low- z . Finally we conclude in Sec. 5.

2 PRELIMINARIES

We first briefly review the ASU picture where we introduce the local comoving coordinate in which the effect of large-scale tidal field is absorbed effectively into the anisotropic expansion. Then we discuss the tidal response function of the matter power spectrum on which we mainly focus in this paper. More detailed discussions can be found in Masaki et al. (2020) (also see Takada & Hu 2013; Akitsu et al. 2017).

2.1 Anisotropic separate universe picture

Let us begin with considering the gravitational potential field that arises from the matter density fluctuations with wavelengths much longer than a survey window W (or a simulation box size). We denote the long-wavelength gravitational field at the position \mathbf{x} as $\Psi^L(\mathbf{x})$. We can Taylor-expand $\Psi^L(\mathbf{x})$ around the center of a survey region, denoted as \mathbf{x}_0 , as

$$\Psi^L(\mathbf{x}) \simeq \Psi^L(\mathbf{x}_0) + \nabla_i \Psi^L|_{\mathbf{x}_0} \Delta x^i + \frac{1}{2} \nabla_i \nabla_j \Psi^L|_{\mathbf{x}_0} \Delta x^i \Delta x^j + \mathcal{O}(\nabla^3 \Psi^L|_{\mathbf{x}_0} \Delta x^3), \quad (1)$$

where $\nabla_i = \partial/\partial x^i$ and $\Delta x^i = x^i - x_0^i$. The second derivative of the potential is so-called the Hessian matrix at the position \mathbf{x}_0 , and can be decomposed into two terms as

$$\nabla_i \nabla_j \Psi^L|_{\mathbf{x}_0} = 4\pi G \bar{\rho} a^2 \left(\frac{1}{3} \delta_{ij}^K \delta_b + K_{ij} \right), \quad (2)$$

where

$$\delta_b \equiv \frac{1}{4\pi G \bar{\rho} a^2} \nabla^2 \Psi^L|_{\mathbf{x}_0}, \quad (3)$$

$$K_{ij} \equiv \frac{1}{4\pi G \bar{\rho} a^2} \left(\nabla_i \nabla_j \Psi^L - \frac{1}{3} \delta_{ij}^K \nabla^2 \Psi^L \right)|_{\mathbf{x}_0}. \quad (4)$$

In the above, we have introduced the mean matter density $\bar{\rho}$ and the scale factor a for the global background cosmology, and δ_{ij}^K is the Kronecker delta function. The trace part of the Hessian matrix is equivalent to δ_b that is the averaged density fluctuation or density contrast over the survey region, and the trace-less part K_{ij} is the supersurvey tidal tensor. Both quantities take constant values over the given survey region by construction and vary only with time: $\delta_b(t)$ and $K_{ij}(t)$. Since we are interested in the impact of K_{ij} on structure formation inside the survey region or a simulation box, we set $\delta_b = 0$ throughout this paper.

Without loss of generality, we can take the coordinate axes of a simulation box to be along the principal axes of the tidal tensor, K_{ij} . In such simulation coordinates, the tidal tensor can be expressed as $K_{ij} \equiv \delta_{ij}^K K_i$, where K_i is the i th eigenvalue ($i = 1, 2$ or 3). If the survey volume or simulation volume is sufficiently large, the supersurvey mode is safely considered to be in the linear regime until today. Under this setting we can have $K_i(t) = D_+(t) \lambda_i$, where D_+ is the linear growth factor normalized as $D_+ = 1$ at present. Hence λ_i stands for the amplitude of the i th tidal eigenvalue at present.

As developed in Masaki et al. (2020), we can absorb the effect of supersurvey tidal tensor into the expansion history of the local volume rather than directly solving the mode

coupling with small-scale modes – so-called anisotropic separate universe picture. To do this, using the Zel'dovich approximation (Zel'dovich 1970), we introduce the anisotropic scale factor a_{W_i} , which describes the effective expansion history of the local volume under the supersurvey tides as

$$a_{W_i}(t) \simeq a(t) [1 - K_i(t)] \equiv a(t) \alpha_{W_i}(t), \quad (5)$$

which is a good approximation for the case of $\lambda_i \ll 1$ (Schmidt et al. 2018; Masaki et al. 2020), and α_{W_i} is the normalized scale factor defined as $\alpha_{W_i} \equiv a_{W_i}/a$. Hereafter, a quantity with subscript W means the quantity in the local coordinates. Since the physical distance has nothing to do with the global or local background expansion, the following relation between the global comoving coordinate x_i and the local comoving coordinate x_{W_i} holds

$$r_i = a(t) x_i = a_{W_i}(t) x_{W_i}. \quad (6)$$

Using the normalized scale factor, the above relation reads $x_i = \alpha_{W_i} x_{W_i}$. Our ASU code solves the gravitational interaction between simulation particles in the local comoving coordinate. Similarly, the wave vectors for the global and the local comoving coordinates are related via

$$k_i = k_{W_i} / \alpha_{W_i}. \quad (7)$$

2.2 The tidal response of the matter power spectrum

The supersurvey tidal tensor is not observable but affects the growth of structures in the local volume through the non-linear mode coupling. One quantity to characterize the impact of the supersurvey tidal tensor is the *response* function of the matter power spectrum that describes how the supersurvey tensor affects the anisotropy in the matter power spectrum as a function of time and scales. A hypothetical observer in the local volume can sample only subsurvey modes of the matter density field, and can measure their power spectrum denoted as $P(\mathbf{k}; K_{ij})$. Due to the trace-less condition of the tidal tensor $\text{Tr}(K_{ij}) = 0$, the supersurvey tidal tensor causes a quadrupolar modulation in the power spectrum depending on the alignments between K_{ij} and the wave vector \mathbf{k} . Thus this effect cannot be studied by the monopole power spectrum, $P(k)$, which is obtained by taking the angle average of the power over a spherical shell of a given radius k . Assuming that the supersurvey tidal tensor is small in amplitude, the observed power spectrum can be Taylor-expanded around $K = 0$ as

$$\begin{aligned} P(\mathbf{k}; K_{ij}) &\simeq P(\mathbf{k}; K_{ij} = 0) + \left. \frac{dP(\mathbf{k}; K_{ij})}{dK_{ij}} \right|_{K_{ij}=0} K_{ij} \\ &= P(k) [1 + R_K(k) \hat{k}_i \hat{k}_j K_{ij}], \end{aligned} \quad (8)$$

where $P(\mathbf{k}; K_{ij} = 0) = P(k)$ is the matter power spectrum in the absence of K_{ij} , i.e. the ensemble-average spectrum of the global background, and $\hat{k}_i \equiv k_i/k$. The factor $R_K(k)$ is the tidal response function defined as

$$R_K(k; t) \hat{k}_i \hat{k}_j \equiv \frac{1}{P(k)} \left. \frac{dP(\mathbf{k}; K_{ij})}{dK_{ij}} \right|_{K_{ij}=0}. \quad (9)$$

The tidal response function $R_K(k)$ describes the response of the power spectrum to the large-scale tidal field as a function of k . Using the growth-dilation derivative technique (Li

et al. 2014; Masaki et al. 2020), the tidal response function is decomposed into two terms:

$$\left. \frac{dP(\mathbf{k}, K_{ij})}{dK_{ij}} \right|_{\mathbf{k}, K_{ij}=0} \simeq \left. \frac{\partial P_W(\mathbf{k}_W, K_{ij})}{\partial K_{ij}} \right|_{\mathbf{k}_W, K_{ij}=0} - \frac{\partial P(k)}{\partial \ln k} \hat{k}_i \hat{k}_j. \quad (10)$$

The first term on the r.h.s is the growth tidal response which describes how the growth of the density perturbation is affected by the supersurvey tidal tensor. The second term is the dilation response which arises from the modulation of wave vector via $k_{Wi} = k_i/\alpha_{Wi}$. We define the growth tidal response function G_K as

$$G_K(k) \hat{k}_i \hat{k}_j \equiv \frac{1}{P(k)} \left. \frac{\partial P_W(\mathbf{k}_W, K_{ij})}{\partial K_{ij}} \right|_{\mathbf{k}_W, K_{ij}=0}. \quad (11)$$

Thus the relation between R_K and G_K is

$$R_K(k) = G_K(k) - \frac{\partial \ln P(k)}{\partial \ln k}. \quad (12)$$

Since the dilation response function $-\partial \ln P(k)/\partial \ln k$ can be evaluated using the standard isotropic simulations, we use the ASU simulations to measure the growth tidal response function G_K .

We use the method developed by Schmidt et al. (2018) to estimate G_K from paired ASU simulations. To do so, we use three simulations, labeled as ‘‘A’’, ‘‘B’’, and ‘‘C’’, for which we generate the initial conditions with the same random seeds. The three runs employ different values for the present-day supersurvey tidal tensor: $\lambda_A = \lambda_{A,z}(-0.5, -0.5, 1)$, $\lambda_B = -\lambda_A$ and $\lambda_C = (0, 0, 0)$, where $\lambda_{A,z}$ is a parameter to fix the tidal tensor amplitude. The estimator of the growth tidal response is given as

$$G_K(k) = \frac{\langle [P_{WA}(\mathbf{k}_{WA}) \mathcal{L}_2(\hat{k}_{WA,z}) - P_{WB}(\mathbf{k}_{WB}) \mathcal{L}_2(\hat{k}_{WB,z})] \rangle}{\langle 2\lambda_{A,z} P_{WC}(\mathbf{k}_{WC}) \mathcal{L}_2^2(\hat{k}_{WC,z}) D_+(t) \rangle}, \quad (13)$$

where $P_{WX}(\mathbf{k}_{WX})$ is the three-dimensional matter power spectrum measured in the local comoving frame for the run X (=A, B, C), $\langle \dots \rangle$ denotes the angle average over a spherical shell of radius k , $\mathcal{L}_2(\mu)$ is the second-order Legendre polynomial; $\mathcal{L}_2(\mu) = (3\mu^2 - 1)/2$. Here μ is the cosine between the z -axis and the wave vector \mathbf{k} . Thus G_K measured using Eq. (13) can be characterized by a single parameter $\lambda_{A,z}$. The value of $\lambda_{A,z}$ should be small such that the higher order corrections do not contribute significantly to the estimator (Eq. 13). We have tried different values in Masaki et al. (2020) and confirmed that the results are converged well by setting $\lambda_{A,z} = 0.01$, which we employ in this work.

3 ASU SIMULATIONS

We describe details of simulations performed in this paper. We first describe the grid and glass pre-ICs to set up initial conditions in an N -body cosmological simulation. Then we present the specifications of our ASU simulations.

3.1 The Pre-ICs

The pre-IC refers to a ‘‘uniform’’ distribution of simulation particles, needed before perturbing positions and assigning

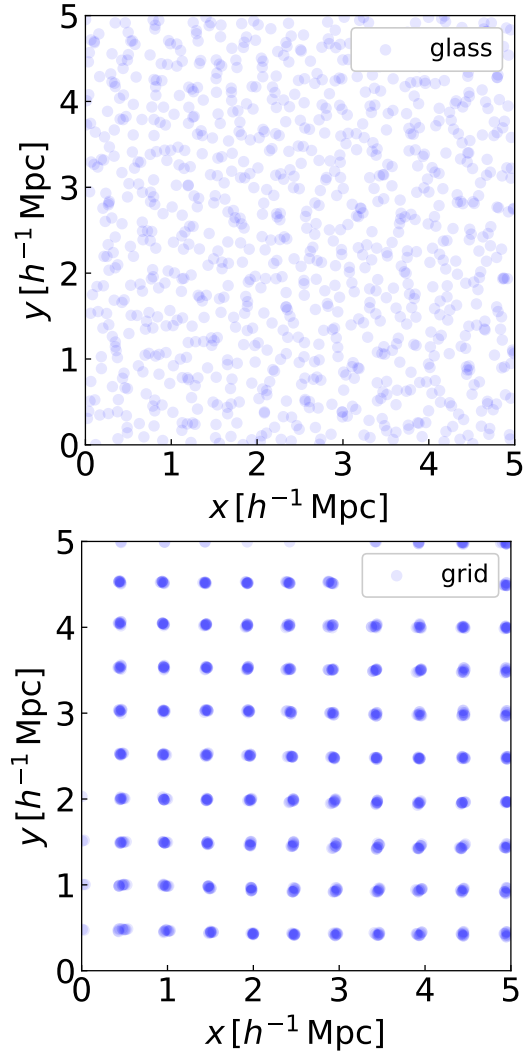


Figure 1. The particle distribution in a subvolume of the initial conditions (ICs) at $z = 63$. Here we consider a cubic subvolume of $5 h^{-1}\text{Mpc}$ on side, and shows the particle distribution projected along one axis. The upper (lower) panel shows the IC generated from the glass (grid) pre-IC. The random seeds are the same for the both ICs; that is, the ICs are the same realization.

velocities for each particle to set up the initial conditions in an N -body simulation. Here, however, a perfectly uniform distribution can never be achieved with a finite number of particles. In this paper, we adopt the grid- or glass-based particle distribution for the pre-ICs to generate the ICs. Figure 1 shows a projected distribution of the particle locations in grid- and glass-based ICs at $z = 63$, where the adopted cosmology (see Sec. 3.2), the total number of particles, and the random initial seeds are exactly the same.

One can easily construct the grid pre-ICs by placing the simulation particles on the lattice evenly spaced in the three-dimensional spatial coordinates (Efstathiou et al. 1985). The grid pre-IC is a conventional method often adopted in the literature, because of the simplicity of implementation and the fast computation. Obviously, the grid-based ICs by construction have intrinsic anisotropies as shown in Figure 1. The anisotropic particle distribution could cause an artifact

in the simulation outputs at a later time; especially it could be so if we want to study anisotropic statistics from simulations. Hence we need to carefully study whether the simulation output at a later time does not depend on the artifacts of initial conditions, e.g. by changing the initial redshifts and the number of particles.

Another configuration we use is the glass pre-ICs (White 1996). One can obtain a glass pre-IC by evolving randomly distributed particles with *anti*-gravity between particles in an expanding background until each particle feels no force from other particles. Whilst its computational cost is relatively high, the particle distribution is expected to suppress intrinsic anisotropy as shown in Figure 1 (see also Liao 2018, for an alternative method using CCVT). In this paper, we use GADGET-2 (Springel et al. 2001; Springel 2005) to generate the glass pre-ICs. We note that the number of particles used in the glass pre-IC is the same as that employed in each simulation (see Sec. 3.2), i.e., we do not tile a glass distribution with a small number of particles to prepare a larger, entire pre-IC.

Thus the grid and glass pre-ICs are considered to be intrinsically anisotropic and nearly isotropic, respectively, on scales of particle separations in the initial conditions. By using both the pre-ICs for ASU, we can assess the impacts of intrinsic anisotropy of pre-ICs on the tidal response measured in simulations.

3.2 ASU simulation specifications

We adopt a flat Λ -cold dark matter (Λ CDM) cosmology that is consistent with the *Planck* 2015 constraint: $\Omega_m = 0.3156$, $\Omega_\Lambda = 0.6844$, $H_0 = 100h = 67.27 \text{ km s}^{-1} \text{ Mpc}^{-1}$, $n_s = 0.9645$ and $A_s = 2.207 \times 10^{-9}$ for the global background (Planck Collaboration et al. 2016). For all the simulations, we take the box size of $L_{\text{box}} = 31.25 h^{-1} \text{ Mpc}$ in the local comoving coordinate. Because we are interested in the k -dependence of G_K on small scales, up to $k \approx 10 h \text{ Mpc}^{-1}$, we adopt the small box size compared to a typical size of cosmological N -body simulations². For both the grid and glass pre-IC configurations, we perform three sets of simulations with different number of particles $N_{\text{part}} = 256^3$, 128^3 or 64^3 . We set the softening parameter to be $\epsilon = 0.05 \times L_{\text{box}}/N_{\text{part}}^{1/3} = 6.1$, 12.2 and $24.4 h^{-1} \text{ kpc}$ and the initial redshift to be $z_{\text{ini}} = 255$, 127 and 63 for $N_{\text{part}} = 256^3$, 128^3 and 64^3 , respectively. We use CAMB (Lewis et al. 2000) to compute the initial matter power spectrum for the global background at redshift $z = z_{\text{ini}}$. We run 16 realizations for each set, assuming three different amplitudes of the supersurvey tidal tensor today, $\lambda_z = 0.01$, -0.01 and 0 for each realization corresponding to the A, B and C runs (see Eq. 13). We thus carry out (2 pre-ICs) \times (3 resolutions) \times (16 realizations) \times (3 tidal fields) = 288 simulations in total.

We use the IC generator and the N -body solver for the ASU simulations developed by Masaki et al. (2020). The IC generator calculates the particle density and velocity fields by the second-order Lagrangian PT (Scoccimarro

1998; Crocce et al. 2006; Nishimichi et al. 2009), and includes the effect of the superbox tidal tensor predicted by PT (Akitsu et al. 2017; Barreira & Schmidt 2017). The N -body simulation code is the modified version of GADGET-2 calculating the gravitational force by the TREEPM algorithm (Bagla 2002), and properly incorporates the anisotropic expansion caused by the tidal field.

4 RESULTS

In this section, we show the main results of this paper that are to compare the tidal responses measured from different redshift outputs of the simulation runs with the grid and glass pre-ICs. For clarification of our demonstration, we show the results for the three regimes of redshifts in separate subsections: we first show the results for very high redshifts at $z \geq 15$, where all the wavelength scales we study are in the linear or quasi non-linear regime, and then the results for $5 \lesssim z \lesssim 9$, where some scales are in the non-linear regime. Finally we show the results at low redshifts $z \leq 3$.

4.1 At $z \geq 15$: a boosted tidal response beyond the PT prediction

First we study the growth response of the matter power spectrum at high redshifts when the matter density fluctuations grow almost linearly over the range of scales we study in this paper. At such high redshifts, we would naively expect that G_K agrees with the PT prediction, i.e. $G_K = 8/7$ (Akitsu et al. 2017; Barreira & Schmidt 2017) over all scales. However, this is not the case as shown below. Figure 2 shows the growth tidal response functions G_K at $z = 31$ and 15 measured from our six simulation sets. According to the resolution study in our previous paper (see Sec. 4.3 in Masaki et al. 2020), we believe that the results for G_K up to $k = 12, 6$ and $3 h \text{ Mpc}^{-1}$ for the sets with $N_{\text{part}} = 256^3$, 128^3 and 64^3 , respectively, are not affected by the numerical resolution eventually at $z = 0$ (see also the discussion below for the transient behavior which depends on the resolution). The error bars are on the mean value, which are evaluated by dividing the standard deviation from the 16 realizations by $\sqrt{16}$. The horizontal thin dotted line denotes the PT prediction. At both redshifts, G_K measured from the six simulation sets agree well with $G_K = 8/7$ at $k \lesssim 1 h \text{ Mpc}^{-1}$. The situation is different at the smaller scales. At $z = 31$, the glass runs with the different particle resolutions agree well with each other and with the PT prediction $G_K = 8/7$. On the other hand, the grid runs display a deviation from the PT prediction $G_K = 8/7$, and the amount of deviation depends on the particle resolution; the lower-resolution run starts to deviate from $G_K = 8/7$ from smaller k -bins, and shows a more significant deviation in the larger k bins. The resolution-dependent behavior for the grid runs should be artificial and likely ascribed to the anisotropic particle distribution due to the grid pre-ICs (also see Stücker et al. 2020, for similar discussion).

At a later time, $z = 15$, G_K from the glass runs now exhibits a deviation from the PT prediction ($8/7$) and an enhanced amplitude compared to $8/7$. The glass results with different resolutions are all consistent with each other, except for $N_{\text{part}} = 128^3$ at the largest wavenumber bin, where a slightly higher amplitude than the highest resolution run,

² We checked that all the results presented below agree with the results from the runs with larger box size of 125 and 500 $h^{-1} \text{ Mpc}$ at each reliable scale range.

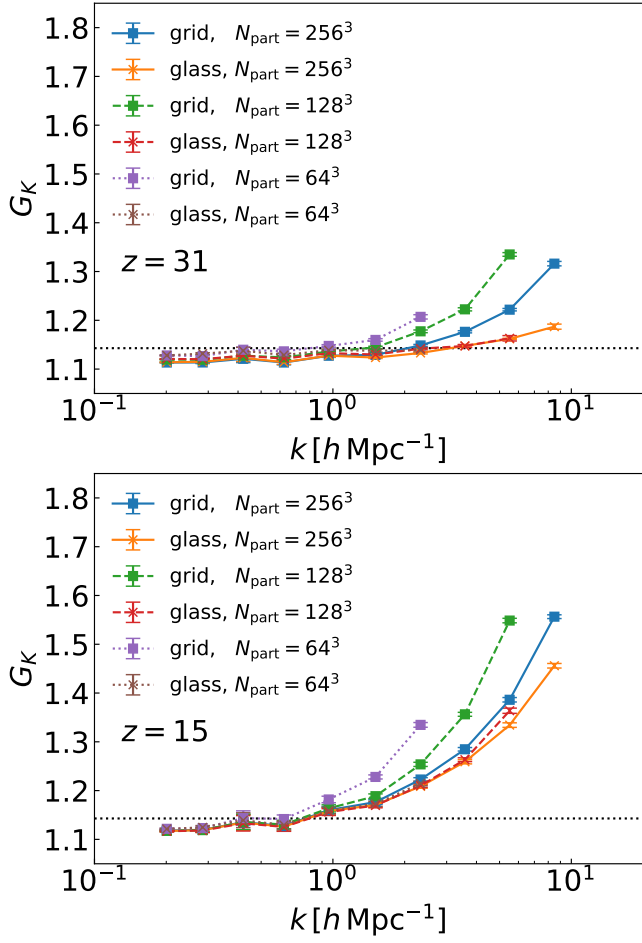


Figure 2. The growth tidal response functions, $G_K(k)$, at $z = 31$ and 15 , respectively, measured from the simulations with the grid- and glass-ICs (see text for details of the measurement method). The horizontal dotted line in each panel denotes the PT prediction $G_K = 8/7$.

$N_{\text{part}} = 256^3$ can be found, indicating that the former might suffer from an inaccuracy due to the insufficient resolution. Nevertheless all the results show the same trend, and we conclude that the enhancement is genuine, and not an artificial feature. The grid runs also show a similar enhancement, although the results show a clear dependence on the resolution at large k bins. The enhancement in the growth response means that the growth of structure formation is enhanced, depending on the degree of alignments between the principal axes of the supersurvey tidal tensor and the small-scale wave vectors \mathbf{k} . This also indicates the importance of tidal field in an early-phase structure formation.

4.2 At $5 \lesssim z \lesssim 9$: from enhancement to suppression in the tidal response

Figure 3 shows G_K at four redshifts, $z = 9.10, 7.66, 6.43$ and 5.37 , from top to bottom, where the four redshifts are chosen such that the logarithmic linear growth rates are evenly spaced. It can be seen that G_K at $z = 9.10$ is more enhanced than at $z = 15$, but the figure shows a similar resolution de-

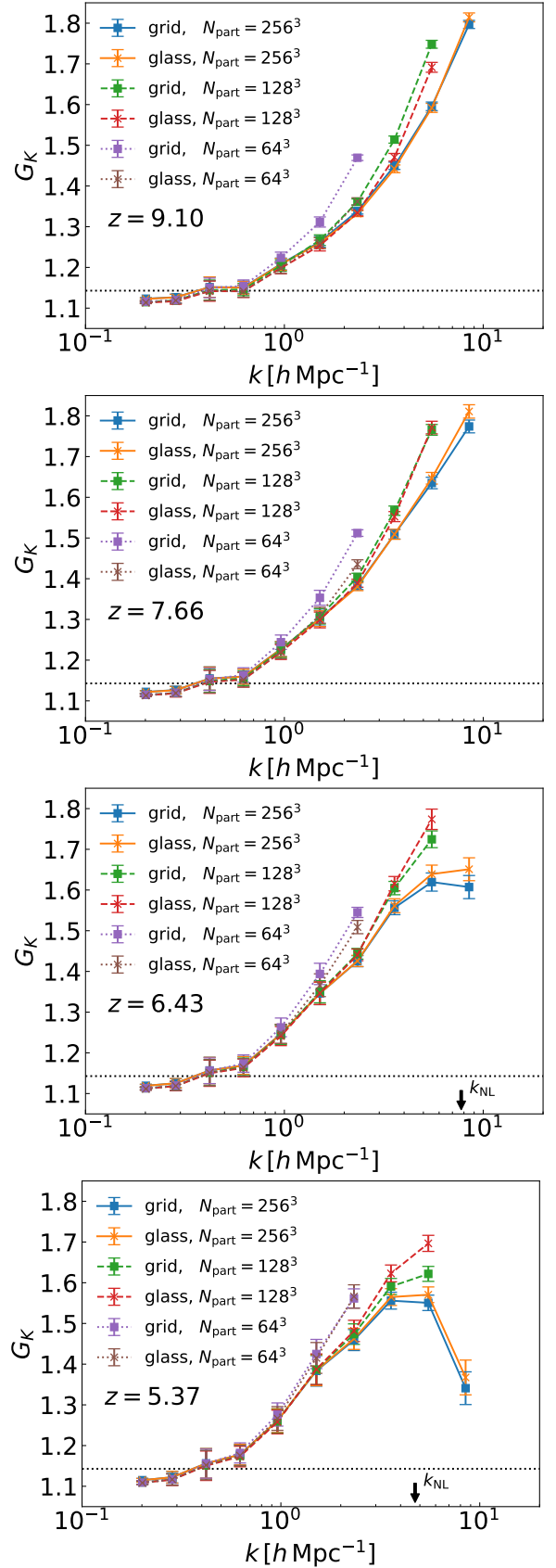


Figure 3. Similar to the previous figure, but here we show G_K at $z = 9.10, 7.66, 6.43$ and 5.37 from top to bottom, respectively. The arrow in the horizontal (x -) axis denotes a scale of k_{NL} below which structures are in the non-linear regime (see Eq. 14 for the definition).

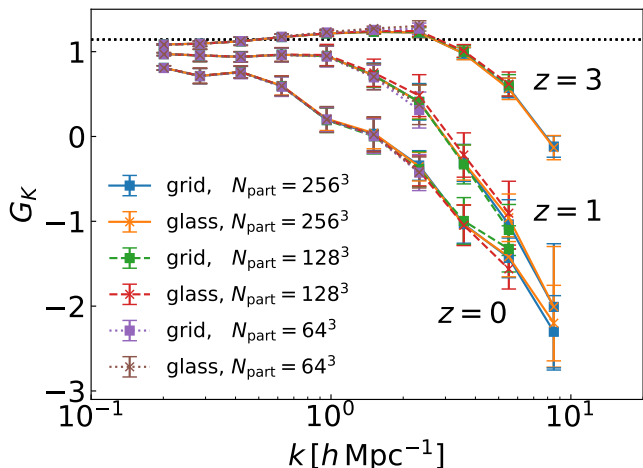


Figure 4. Similar to Figure 2, but for G_K at $z = 3, 1$ and 0 .

pendence for the grid runs to those in Figure 2. A similar, but weaker trend with resolution can be found among the simulations with glass pre-ICs, unlike the results at higher redshifts. We also note that the pre-IC dependence becomes very weak for the highest and the middle resolution runs implying that G_K is losing the memory of pre-ICs at around this time. At $z = 7.66$, the overall amplitudes are similar to $z = 9.10$ but the slopes at $k \gtrsim 1 h \text{ Mpc}^{-1}$ for the highest resolution runs become shallower. As structures grow and the non-linearities evolve towards lower redshifts, the G_K amplitude starts to saturate at a certain k , and then decreases at the higher k . Thus we can expect that the G_K amplitude is in its peak around $z \approx 8$ for the fiducial ΛCDM model.

The suppression at $k \gtrsim 3 h \text{ Mpc}^{-1}$ for the highest resolution runs can be seen clearly at $z = 6.43$. The suppression would be due to formation of non-linear structures such as halos because such non-linear structures likely reduce the coupling with the large-scale tidal field. This interpretation is supported by the fact that the suppression of G_K occurs at around the non-linear scale k_{NL} defined as

$$\Delta^2(k_{\text{NL}}) \equiv \frac{k_{\text{NL}}^3 P(k_{\text{NL}})}{2\pi^2} = 1. \quad (14)$$

To compute k_{NL} , we use the non-linear matter power spectrum calculated with the revised HALOFIT fitting formula (Takahashi et al. 2012). We also have checked that the matter power spectrum measured in the simulations at $z = 7$ already deviates from the linear prediction displaying the non-linear feature at $k \gtrsim 1 h \text{ Mpc}^{-1}$. For the lower resolution runs, such a suppression is not seen because the lower resolution runs cannot resolve small halos at such high-redshift. At later time, $z = 5.37$, more massive halos form. Hence the suppression is stronger for the highest resolution runs, and can be seen even for the middle resolution runs. Similarly to the results at $z = 6.43$, the suppression is seen around $k = k_{\text{NL}}$.

4.3 At $z \leq 3$: suppression due to non-linear clustering

Figure 4 is similar to the previous figures but for G_K at $z = 3, 1$ and 0 now shown together in one panel. On the contrary to higher- z , G_K are more suppressed at smaller scales due to the non-linear evolution of matter clustering. At $z \leq 3$, the resolution dependence seen at $z \gtrsim 5$ is no longer observed. This would be because massive halos, which can be resolved even by the lower resolution sets, form and give the dominant contribution to the suppression. As shown in the figure, the pre-IC effects found at $z \gtrsim 9$ disappear at $z \leq 3$. Thus the growth tidal response at $z \leq 3$, at which the galaxy surveys target, can be measured robustly against for the choice of the pre-IC up to $k = 10 h \text{ Mpc}^{-1}$.

5 CONCLUSION AND DISCUSSION

We have studied the impacts of the intrinsic anisotropy in the particle distribution of the pre-ICs on the growth tidal response function G_K measured in the ASU simulations. To do so, we have used the grid pre-ICs, which have intrinsically anisotropic particle distributions, and the glass pre-ICs, in which particles distribute nearly isotropically (see Figure 1). Using the both pre-ICs, we have carried out the ASU simulations with the IC generator and N -body solver code developed by Masaki et al. (2020), and then compared the measured G_K through the cosmic time. Analysing carefully the results at different redshifts, we have aimed at disentangling the artifacts due to the anisotropies in the pre-ICs and the mere lack of resolution at different stages of structure formation.

We have shown that G_K measured from the grid pre-IC runs at $z \geq 15$ exhibit an artificial, apparent enhancement in the amplitude at small scales depending on the particle resolution, which is ascribed to a numerical inaccuracy due to the artificial anisotropy in the grid pre-ICs, at smaller scales depending on the particle resolution (Figure 2). On the other hand, the glass pre-ICs simulations also display an enhanced amplitude in the response compared to the PT prediction ($G_K = 8/7$), whose magnitude is insensitive to the particle resolutions. Hence, we conclude that the enhancement of G_K in such high redshifts is not an artifact, and genuine implying the importance of large-scale tidal field in an early-phase structure formation. The pre-IC dependence becomes smaller at $z \lesssim 9$ (Figure 3). We also showed that the G_K amplitude has a turn-around around the non-linear scale k_{NL} , which is defined by $k^3 P(k)/2\pi^2|_{k=k_{\text{NL}}} = 1$, and then starts to decrease at larger k . Therefore, from this stage, the measured G_K function starts to behave differently depending on the resolving power of the simulation. At $z \leq 3$, the impacts of the pre-ICs are negligible (Figure 4), since the dominant contributor to the G_K function is massive halos, which can be resolved even in the poorest-resolution simulations presented in this paper.

Wang & White (2007) pointed out a possible artifact in simulations with the glass pre-ICs for warm dark matter cosmologies, instead of CDM, where they found a spurious fragmentation of filaments. For this, Liao (2018) showed that the power spectrum measured from the particle distribution in the CCVT pre-ICs is closer to the minimal spectrum $P(k) \propto k^4$ (Peebles 1980) than seen in the glass pre-ICs

which are generated by GADGET-2. To study the impacts of a possible imperfection of the glass pre-ICs, we additionally carried out the simulations with the same setting, but using the CCVT pre-ICs³. We found that all the results from the CCVT pre-ICs are almost identical to those from the glass pre-ICs. Therefore we conclude that the glass pre-ICs are sufficient for our purpose, at least for the CDM cosmologies. As clearly demonstrated in these analyses, the tidal response function at high redshifts is a good example where an appropriate choice of pre-ICs is crucial, and the conventional grid pre-IC could lead to an inaccurate estimate.

An interesting implication of our findings is that the growth response G_K has a maximum amplitude around $z \sim 8$, which is during EoR. This implies that structure formations during the EoR era has a stronger coupling with the large-scale tidal field. In other words statistical quantities in the EoR era can be used to study the large-scale tidal field. One interesting possibility is that large-scale structures in the EoR era might give an enhanced sensitivity to the anisotropic primordial non-Gaussianity, if an appropriate observable, galaxy shapes or shapes of large-scale structure in the EoR era, is identified (Akitsu et al. 2020). On theory side, our results imply that it is important to take into account the superbox tidal field, based on the anisotropic separate universe technique, when simulating structure formation with an extremely small size box. Separate universe simulation technique is powerful and useful to incorporate environmental effects. Recently, D’Aloisio et al. (2020) studied the evolution of inter-galactic medium (IGM) and its impacts on reionization using the radiation-hydrodynamics cosmological simulations in the separate universe simulation. Their simulations employ relatively small box sizes of $\mathcal{O}(1) h^{-1}$ Mpc but incorporates the environmental effects by including the large-scale density contrast δ_b (Sirko 2005; Gnedin et al. 2011; Li et al. 2014). They found significant impacts of δ_b on the gas distribution during the EoR era. Since the density contrast δ_b and the tidal field K_{ij} are both from the Hessian matrix of the long-wavelength gravitational potential, δ_b and K_{ij} should be equally important. It would be interesting to study the impacts of K_{ij} on the IGM evolution and the reionization physics. This could be our future work.

ACKNOWLEDGEMENTS

All the simulations were carried out on Cray XC50 at Center for Computational Astrophysics, National Astronomical Observatory of Japan. We would like to thank Fabian Schmidt for useful discussion. We would like to appreciate Shihong Liao for making their codes and pre-IC data publicly available. This work was supported in part by World Premier International Research Center Initiative (WPI Initiative), MEXT, Japan, JSPS KAKENHI Grant Numbers JP15H03654, JP15H05887, JP15H05893, JP15H05896, JP15K21733, JP17K14273 and JP19H00677, and by JST AIP Acceleration Research Grant Number JP20317829, Japan.

³ We used the CCVT pre-IC data publicly available at <https://github.com/liaoshong/ccvt-preic-data>.

DATA AVAILABILITY

The data used in this paper will be provided by the authors upon request.

REFERENCES

- Aihara H., et al., 2018, *PASJ*, **70**, S4
Akitsu K., Takada M., 2018, *Phys. Rev. D*, **97**, 063527
Akitsu K., Takada M., Li Y., 2017, *Phys. Rev. D*, **95**, 083522
Akitsu K., Kurita T., Nishimichi T., Takada M., Tanaka S., 2020, arXiv e-prints, p. [arXiv:2007.03670](https://arxiv.org/abs/2007.03670)
Bagla J. S., 2002, *Journal of Astrophysics and Astronomy*, **23**, 185
Baldauf T., Seljak U., Senatore L., Zaldarriaga M., 2016, *J. Cosmology Astropart. Phys.*, **2016**, 007
Barreira A., Schmidt F., 2017, *J. Cosmology Astropart. Phys.*, **2017**, 053
Barreira A., Nelson D., Pillepich A., Springel V., Schmidt F., Pakmor R., Hernquist L., Vogelsberger M., 2019, *MNRAS*, **488**, 2079
Barreira A., Cabass G., Schmidt F., Pillepich A., Nelson D., 2020, arXiv e-prints, p. [arXiv:2006.09368](https://arxiv.org/abs/2006.09368)
Baugh C. M., Gaztanaga E., Efstathiou G., 1995, *MNRAS*, **274**, 1049
Chan K. C., Li Y., Biagetti M., Hamaus N., 2020, *ApJ*, **889**, 89
Crocce M., Pueblas S., Scoccimarro R., 2006, *Mon. Not. Roy. Astron. Soc.*, **373**, 369
D’Aloisio A., McQuinn M., Trac H., Cain C., Mesinger A., 2020, arXiv e-prints, p. [arXiv:2002.02467](https://arxiv.org/abs/2002.02467)
Efstathiou G., Davis M., White S. D. M., Frenk C. S., 1985, *ApJS*, **57**, 241
Gnedin N. Y., Kravtsov A. V., Rudd D. H., 2011, *ApJS*, **194**, 46
Hamilton A. J. S., Rimes C. D., Scoccimarro R., 2006, *MNRAS*, **371**, 1188
Hansen S. H., Agertz O., Joyce M., Stadel J., Moore B., Potter D., 2007, *The Astrophysical Journal*, **656**, 631–635
Ip H. Y., Schmidt F., 2017, *J. Cosmology Astropart. Phys.*, **2017**, 025
Joyce M., Marcos B., 2007, *Phys. Rev. D*, **76**, 103505
Joyce M., Marcos B., Baertschiger T., 2009, *Monthly Notices of the Royal Astronomical Society*, **394**, 751–773
L’Huillier B., Park C., Kim J., 2014, *New Astron.*, **30**, 79
Laureijs R., et al., 2011, preprint, ([arXiv:1110.3193](https://arxiv.org/abs/1110.3193))
Lewis A., Challinor A., Lasenby A., 2000, *Astrophys. J.*, **538**, 473
Li Y., Hu W., Takada M., 2014, *Phys. Rev. D*, **89**, 083519
Li Y., Schmittfull M., Seljak U., 2018, *J. Cosmology Astropart. Phys.*, **2018**, 022
Liao S., 2018, *MNRAS*, **481**, 3750
Marcos B., Baertschiger T., Joyce M., Gabrielli A., Sylos Labini F., 2006, *Phys. Rev. D*, **73**, 103507
Masaki S., Nishimichi T., Takada M., 2020, *MNRAS*, **496**, 483
Nishimichi T., et al., 2009, *Publ. Astron. Soc. Japan*, **61**, 321
Peebles P. J. E., 1980, The large-scale structure of the universe
Planck Collaboration et al., 2016, *A&A*, **594**, A13
Sato M., Hamana T., Takahashi R., Takada M., Yoshida N., Matsumura T., Sugiyama N., 2009, *Astrophysical J.*, **701**, 945
Schmidt A. S., White S. D. M., Schmidt F., Stücker J., 2018, *MNRAS*, **479**, 162
Scoccimarro R., 1998, *Mon. Not. Roy. Astron. Soc.*, **299**, 1097
Sirko E., 2005, *ApJ*, **634**, 728
Spergel D., et al., 2015, arXiv e-prints, p. [arXiv:1503.03757](https://arxiv.org/abs/1503.03757)
Springel V., 2005, *Mon. Not. Roy. Astron. Soc.*, **364**, 1105
Springel V., Yoshida N., White S. D. M., 2001, *New Astron.*, **6**, 79
Stücker J., Schmidt A. S., White S. D. M., Schmidt F., Hahn O., 2020, arXiv e-prints, p. [arXiv:2003.06427](https://arxiv.org/abs/2003.06427)

- Takada M., Hu W., 2013, *Phys. Rev. D*, **87**, 123504
Takada M., et al., 2014, *PASJ*, **66**, R1
Takahashi R., Sato M., Nishimichi T., Taruya A., Oguri M., 2012, *ApJ*, **761**, 152
Takahashi R., Nishimichi T., Takada M., Shirasaki M., Shiroyama K., 2019, *MNRAS*, **482**, 4253
Wagner C., Schmidt F., Chiang C. T., Komatsu E., 2015, *MNRAS*, **448**, L11
Wang J., White S. D. M., 2007, *MNRAS*, **380**, 93
White S. D. M., 1993, arXiv e-prints, pp astro-ph/9410043
White S. D. M., 1996, in Schaeffer R., Silk J., Spiro M., Zinn-Justin J., eds, *Cosmology and Large Scale Structure*. p. 349
Zel'dovich Y. B., 1970, *A&A*, **5**, 84

This paper has been typeset from a $\text{\TeX}/\text{\LaTeX}$ file prepared by the author.